Journal of Energy Chemistry 107 (2025) 252–259

Contents lists available at ScienceDirect

Journal of Energy Chemistry

journal homepage: www.elsevier.com/locate/jechem

http://www.journals.elsevier.com/journal-of-energy-chemistry/

Axial coordination engineering of cobalt phthalocyanine enables efficient CO_2 electrolysis to CO ☆

Yawei Hong [a], Chunxiao Liu [a], Chengbo Li [a], Haoyuan Wang [a], Yuan Ji [a], Xinyan Zhang [a], Yujing Ren [c], Zhaoyang Chen [a], Qisheng Zeng [a], Qiu Jiang [a,b], Tingting Zheng [a], Kun Jiang [d], Xu Li [a,*], Chuan Xia [a,b,*]

[a] School of Materials and Energy, University of Electronic Science and Technology of China, Chengdu 611731, Sichuan, China
[b] Yangtze Delta Region Institute (Huzhou), University of Electronic Science and Technology of China, Huzhou 313001, Zhejiang, China
[c] Interdisciplinary Research Center of Biology & Catalysis, School of Life Sciences, Northwestern Polytechnical University, Xi'an 710072, Shaanxi, China
[d] Interdisciplinary Research Center, School of Mechanical Engineering, Shanghai Jiao Tong University, Shanghai 200240, China

ARTICLE INFO

Article history:
Received 6 February 2025
Revised 15 March 2025
Accepted 16 March 2025
Available online 01 April 2025

Keywords:
Molecular catalysts
Axial coordination
Electrochemical CO_2 reduction
Cobalt phthalocyanine

ABSTRACT

Electrocatalytic CO_2-to-CO conversion is crucial for advancing sustainable processes, and providing essential feedstocks for the chemical industry. Cobalt phthalocyanine (CoPc) is a well-established molecular catalyst for this conversion; however, maintaining high selectivity at industrially relevant current densities remains a significant challenge. Herein, we present a Co–N_5 local structure anchored on nitrogen-doped carbon nanotubes through axial nitrogen coordination engineering to CoPc (CoPc/N-CNTs). The catalyst demonstrates near-unity CO selectivity and a high CO turnover frequency, peaking at 19.2 s^{-1} across a wide range of overpotentials. In flow cell tests, CoPc/N-CNTs achieve a CO Faradaic efficiency exceeding 95% at a current density of −800 mA cm^{-2}. When integrated into a membrane electrode assembly, it maintained over 90% CO Faradaic efficiency at an industrial-scale current of −5 A for up to 20 h. Mechanistic studies revealed that Co–N_5 active sites accelerate *COOH formation and inhibit deeper *CO reduction to CH_3OH while reducing HER activity by lowering H_2O surface coverage. These findings offer a delicate catalyst design that enables the efficient and sustained conversion of CO_2 to CO.
© 2025 Science Press and Dalian Institute of Chemical Physics, Chinese Academy of Sciences. Published by Elsevier B.V. and Science Press. All rights are reserved, including those for text and data mining, AI training, and similar technologies.

1. Introduction

The urgent need to address rising carbon dioxide (CO_2) levels, driven by the burning of fossil fuels, has pushed CO_2 conversion technologies to the forefront of sustainable innovation [1]. Electrochemical CO_2 reduction (CO_2RR), which transforms CO_2 into valuable products using renewable electricity, offers a direct route to mitigate carbon emissions while producing chemicals and fuels essential to industry [2,3]. Among these products, carbon monoxide (CO) plays a critical role as a key feedstock in the production of chemicals, metals, and fertilizers [4]. In particular, CO serves as an important precursor for synthesizing hydrocarbons, alcohols, and other compounds through processes such as Fischer-Tropsch synthesis [5]. The broad industrial relevance of CO positions CO_2-to-CO conversion as a high-impact solution for addressing both environmental concerns and industrial demands [6–10].

Despite its potential, electrocatalytic CO_2-to-CO conversion faces significant technical hurdles. The central challenge lies in designing efficient catalysts that exhibit high activity, minimize energy consumption, and avoid unwanted side reactions [11–14]. Generally, CO_2-to-CO conversion follows a two-electron, two-proton transfer mechanism [15,16]. This process starts with the formation of a $*CO_2\bullet-$ radical anion on the catalyst surface, followed by proton transfer to generate a *COOH intermediate. Subsequent proton and electron transfers produce *CO and H_2O [16]. Since the transformation of *COOH into *CO is energetically favorable, optimizing CO production depends on lowering the energy barrier for *COOH formation. Additionally, catalysts must interact weakly with the CO product to enable its rapid desorption and prevent further reduction [17].

Single-atom catalysts (SACs) have attracted considerable attention because of their maximized atomic efficiency, well-defined active sites, and high catalytic selectivity [18]. However, traditional

☆ This article is part of a special issue entitled: 'Electrifying Chemical Industry' published in Journal of Energy Chemistry.

* Corresponding authors.
E-mail addresses: xuli@uestc.edu.cn (X. Li), chuan.xia@uestc.edu.cn (C. Xia).

https://doi.org/10.1016/j.jechem.2025.03.036
2095-4956/© 2025 Science Press and Dalian Institute of Chemical Physics, Chinese Academy of Sciences. Published by Elsevier B.V. and Science Press. All rights are reserved, including those for text and data mining, AI training, and similar technologies.

synthesis methods, such as high-temperature pyrolysis, often encounter issues such as scalability, inconsistent reproducibility, and stringent reaction conditions, limiting their broader industrial application [19]. Cobalt phthalocyanine (CoPc), which consists of a planar framework in which a central cobalt atom is coordinated by four pyridine carbonyl groups connected through benzene linkages, is one of the promising catalysts with well-defined structure for CO_2-to-CO conversion. Its well-defined and tunable molecular structure allows for the precise optimization of CO_2RR pathways [20]. Axial coordination engineering is a promising strategy to increase the activity of metal phthalocyanine catalysts [20–22], utilizing groups such as doped nitrogen, amino, or carboxyl functional groups on carbon supports. However, previous CoPc-based systems face low selectivity and degradation at high current densities, especially those above −400 mA cm^{-2} [20,23–29]. This highlights the pressing need for further advancements in catalyst design to improve both selectivity and stability under industrially relevant conditions.

Herein, we present a novel approach to overcoming these limitations by immobilizing CoPc onto nitrogen-functionalized carbon nanotubes (N-CNTs), creating a catalyst composed of single Co centers coordinated with five N atoms (CoPc/N-CNTs). The use of CNTs as support for molecular catalysts in the field of CO_2RR has applications that far exceed those of other carbon materials, such as graphene, due to their good conductivity and enhancement of mass transfer [23,30–33]. In the Co–N_5 structure, four planar N atoms originate from the phthalocyanine ligand, whereas the axial nitrogen is contributed by the doped N on the CNTs. This axial coordination forms a stable and active Co–N_5 site, significantly enhancing the catalytic performance over that of the conventional CoPc/CNT system. Through comprehensive kinetic experiments, we determined that axial N coordination alters the rate-determining step (RDS) of the Co single atom in the CO_2RR, from the protonation of $*CO_2^-$ to the first electron transfer step, thereby revealing the intriguing outstanding performance of the Co center. The Co–N_5 catalyst achieves over 95% Faradaic efficiency (FE) for CO at −800 mA cm^{-2} in a flow cell and demonstrates excellent stability, operating for over 50 h at a current density of −100 mA cm^{-2} without significant degradation. To validate the scalability and industrial relevance of this catalyst, we expanded the electrode area to 50 cm^2 using an anion exchange membrane electrode assembly (MEA). Under continuous operation at a total current of −5 A, the FE for CO remains stable at approximately 90% over 20 h, demonstrating the robustness of the catalyst at larger scales. By further integrating catalysts into a tandem MEA setup, we observe a sustained CO selectivity of approximately 80% even at a total current of −15 A, highlighting its potential for industrial-scale CO_2 reduction.

2. Results and discussion

2.1. Catalysts preparation and characterization

The CoPc/N-CNTs catalyst was synthesized through a combination of high-temperature pyrolysis and interactions between molecular catalysts and supports (Fig. 1a). First, CNTs were oxidized (O-CNTs) to increase their defect density and enhance their N doping capacity during subsequent treatment. X-ray photoelectron spectroscopy (XPS) confirmed this, revealing a higher nitrogen content on the pretreated CNTs (Fig. S1a, b). XPS of nitrogen 1*s* verified the absence of residual nitrate in the oxidized CNTs (Fig. S1c). Then, nitrogen-doped CNTs were prepared *via* pyrolysis, creating a support enriched with nitrogen atoms. XPS revealed that the predominant forms of nitrogen doping in the N-doped CNTs were graphitic nitrogen, pyridine nitrogen, and nitrogen oxide (Fig. S1c). Finally, the Co–N_5 structure was formed by the coordination of the Co atom in CoPc with the N on the support. As a control, CoPc/CNTs were synthesized using the same method but with undoped CNTs as the support. Since the N-doping treatment was conducted under harsh reductive conditions, unlike in the MOF-based system [21], oxygen species were removed (Fig. S1d), and only adsorbed oxygen species were detected by XPS in both pristine and N-doped CNTs [34], ruling out the possibility of oxygen coordination with Co atoms. The loadings of cobalt (Co) in the two samples were quantified using inductively coupled plasma optical emission spectroscopy (ICP-OES), which were 0.805 wt% for CoPc/N-CNTs and 0.861 wt% for CoPc/CNTs. High-angle annular dark-field scanning transmission electron microscopy (HAADF-STEM) images revealed no significant change in the CNT structure after synthesis (Fig. S2), with diameters ranging from 10 to 20 nm. X-ray diffraction (XRD) analysis confirmed that there was no cobalt metal aggregation or obvious change in the CNTs during synthesis (Fig. S3). HAADF-STEM images and electron microscopy energy-dispersive X-ray spectroscopy (EDS) mapping further demonstrated the uniform distribution of Co, N, and C atoms in the CNTs, with Co atoms appearing monodispersed (Fig. 1b, c). Similarly, CoPc/CNTs displayed a uniform distribution of elements and singly dispersed Co atoms (Fig. S4).

To further investigate the interaction between the cobalt atom in CoPc and the N on the support, a comprehensive characterization was conducted. XPS analysis (Fig. 1d) revealed a significant shift in the binding energy (0.7 eV) of Co 2*p* to a greater value in CoPc/N-CNTs than in CoPc/CNTs and pure CoPc, suggesting strong Co–N interactions in CoPc/N-CNTs. The Co valence increased after N axial coordination due to the high electronegativity of the N atoms. The nitrogen XPS signals of CoPc/N-CNTs were attributed mainly to CoPc, since the amount of N in the loaded CoPc (6.4 wt %) was far greater than that in the doped N determined by XPS (2.2 wt%). The results revealed that the Co—N peak area of CoPc/N-CNTs is significantly larger than those of pure CoPc and CoPc/CNTs, likely due to the axial coordination between doped N and Co atoms, which increases the number of Co—N bonds (Fig. S5). This strong interaction is further supported by the redshift of the Q-band in the UV–vis spectrum, indicating potential charge transfer between CoPc and the support (Fig. S6) [33]. Furthermore, X-ray absorption near-edge structure (XANES) analysis of the Co *K*-edge in CoPc/N-CNTs (Fig. 1e) revealed a slight shift towards higher energy, implying a higher valence state for the Co atoms than those in CoPc/CNTs and CoPc. The Co *K*-edge XANES spectrum features a pronounced peak at 7716 eV, associated with the 1*s* to 4p_z transition typical of the Co–N_4 structure [33]. Notably, the peak intensity from CoPc to CoPc/CNTs and CoPc/N-CNTs decreases gradually, suggesting that axial nitrogen coordination may reduce the symmetry of the Co—N_4 structure [33,35]. Extended X-ray absorption fine structure (EXAFS) analysis and fitting (Fig. 1f, g and Table S1) further confirmed a Co—N coordination number of 5, with the axially coordinated Co—N (Co—N_{axial}) bond length (2.32 Å) being longer than that in CoPc (1.89 Å). These findings collectively suggest that the CoPc/N-CNTs catalyst features a single Co atom that is planarly coordinated with four nitrogen atoms and axially coordinated with a fifth nitrogen atom on the N-CNTs.

2.2. CO_2RR performance

The CO_2RR performance of the catalysts was initially assessed in a three-electrode H-type electrochemical cell using 0.5 M $KHCO_3$ electrolyte. The catalysts were immobilized on a mirror-polished glassy carbon electrode (GCE). The gas products were analyzed *via* gas chromatography (GC), whereas the liquid products were examined using H nuclear magnetic resonance (^{1}H NMR) spectroscopy [36]. Control experiments confirmed that neither the

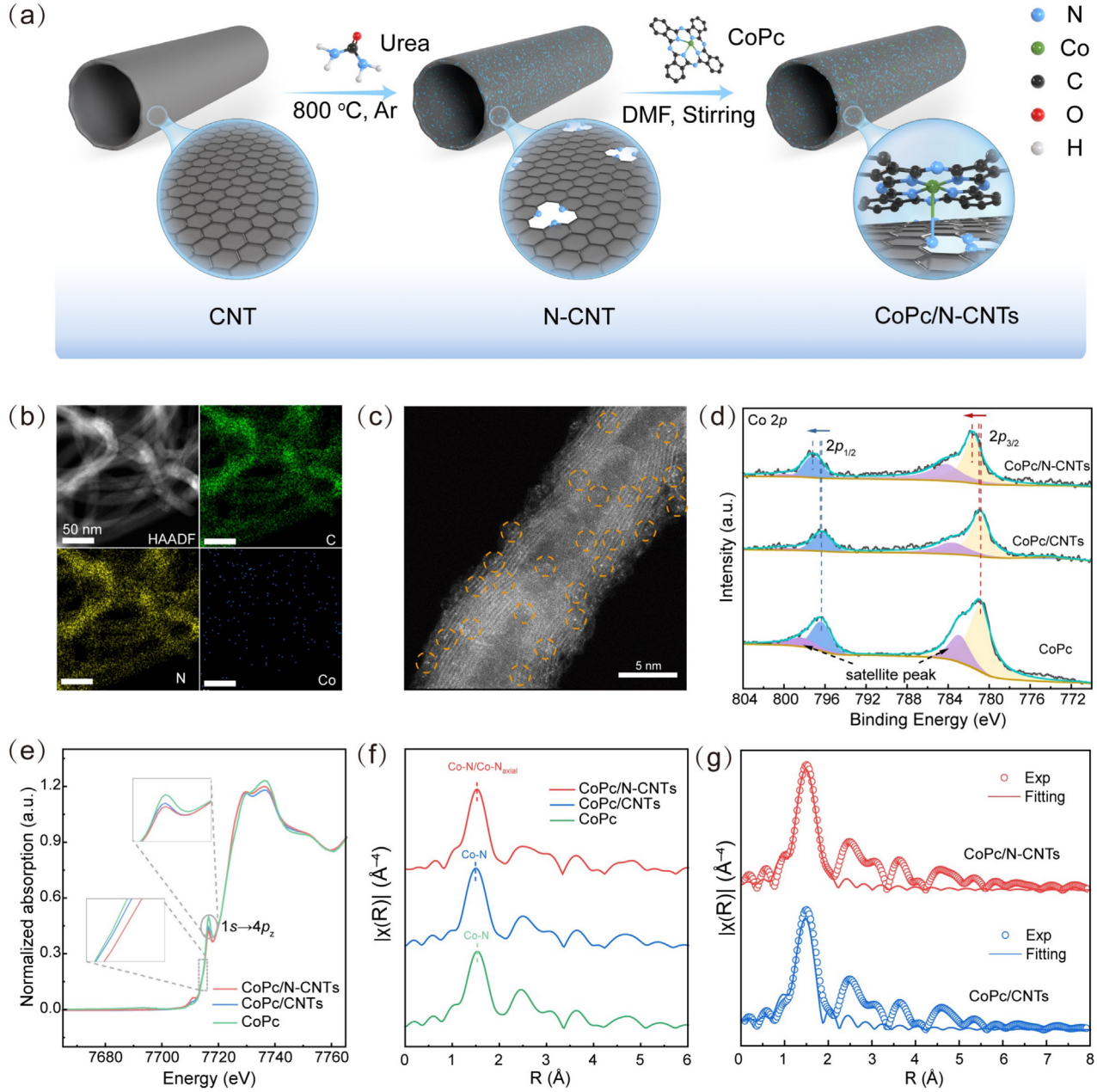

Fig. 1. (a) Schematic of the synthetic procedure and structure of CoPc/N-CNTs. (b) HAADF-STEM image and corresponding EDS images showing the elemental mapping of C, N, and Co in CoPc/N-CNTs. (c) HAADF-STEM image of CoPc/N-CNTs showing the isolated cobalt atoms on the N-CNT surface. (d) XPS of Co 2*p* for CoPc, CoPc/CNTs, and CoPc/N-CNTs. (e) XANES Co *K*-edge spectra of CoPc, CoPc/CNTs, and CoPc/N-CNTs. (f) Fourier transform EXAFS. (g) EXAFS fitting in *R* space of CoPc/CNTs and CoPc/N-CNTs.

CNTs nor the N-CNTs support contributed to the CO_2RR (Fig. S7). On the basis of the combined ^{1}H NMR and GC results, both CoPc/N-CNTs and CoPc/CNTs exhibited more than 80% FE for CO below –0.67 V vs. the reversible hydrogen electrode (RHE). At –0.72 V vs. RHE, CoPc/N-CNTs maintained approximately 85% of the FE_{CO}, whereas the CO FE of CoPc/CNTs decreased to 60%, with a 24% FE for CH_3OH. When the potential was further increased to –0.81 V vs. RHE, CoPc/CNTs presented a greater than 50% FE for H_2, whereas CoPc/N-CNTs presented a 28% H_2 FE, with no CH_3OH production at any potential (Fig. 2a, b, Figs. S8 and S9). Notably, at –0.77 V vs. RHE, CoPc/N-CNTs presented a CO partial current density three times greater than that of CoPc/CNTs, with nearly 100% CO_2-to-CO selectivity (Fig. 2c).

To further evaluate the intrinsic activities of CoPc/N-CNTs and CoPc/CNTs for the CO_2RR, we calculated the CO production turnover frequency (TOF) on the basis of the total amount of loaded Co atoms (see details in the Experimental Section). The maximum TOF of CoPc/N-CNTs (19.2 s^{-1}) was found to be twice that of CoPc/CNTs (9.1 s^{-1}) (Fig. 2d). Measurements of the electrochemically active surface area (ECSA) revealed that the two catalysts had similar ECSAs (Fig. S10), also indicating a much higher intrinsic activity of CoPc/N-CNTs. To assess the long-term stability of CoPc/N-CNTs, a continuous electrocatalytic test was conducted at –10 mA cm^{-2}. After 100 h of operation, the potential was changed from –0.50 to –0.53 V vs. RHE, an increase of only 30 mV, whereas the FE for CO remained at approximately 95% without any loss, demonstrating excellent intrinsic stability (Fig. 2e).

To evaluate the efficacy of the as-prepared catalysts for potential industrial application, we tested the catalysts in a three-electrode flow cell under identical conditions, eliminating

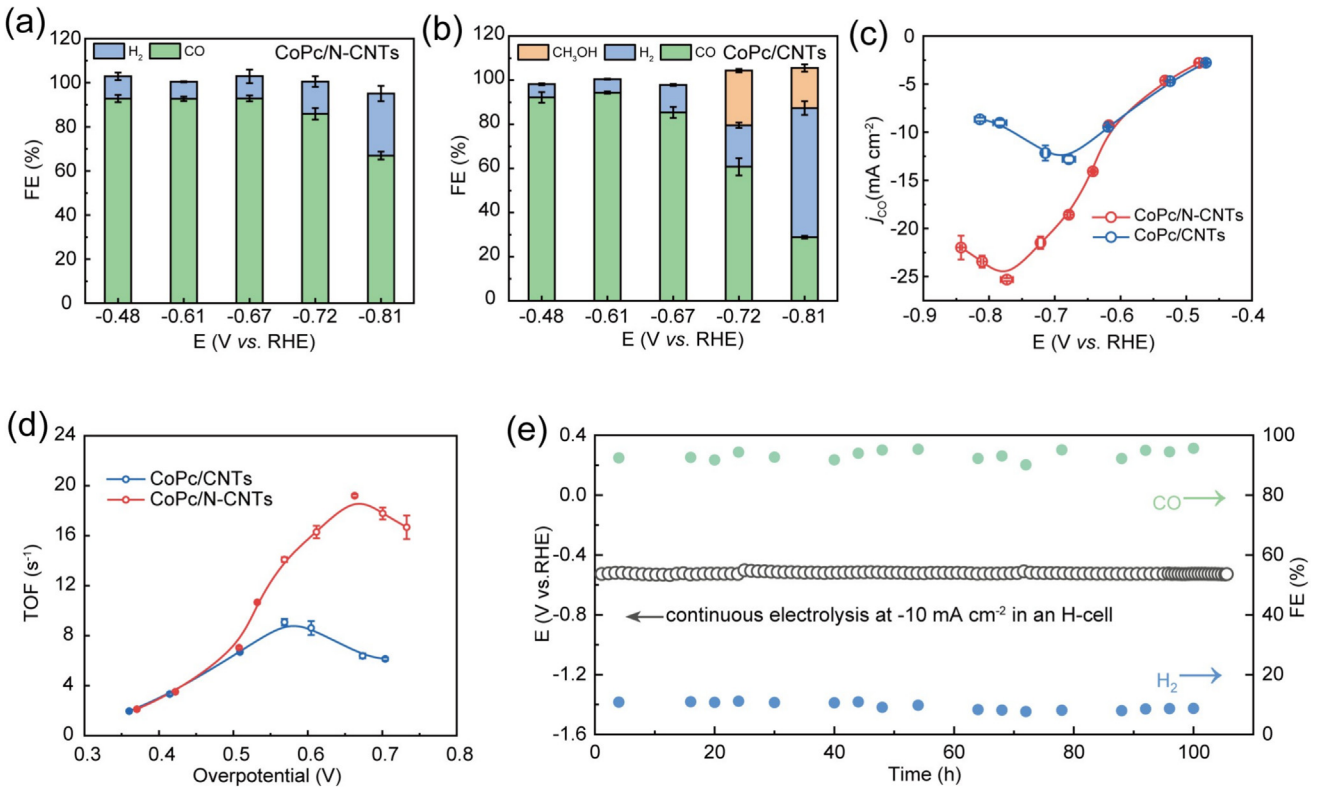

Fig. 2. (a–d) CO_2 electroreduction performance in an H-cell. (a, b) FEs of all CO_2RR products at different potentials of CoPc/N-CNTs and CoPc/CNTs. (c) j_{CO} values of CoPc/N-CNTs and CoPc/CNTs. (d) CO production TOFs of CoPc/N-CNTs and CoPc/CNTs. The mass loading of both catalysts was ~0.5 mg cm^{-2}. (e) CO_2RR stability test of CoPc/N-CNTs at −10 mA cm^{-2}.

CO_2 diffusion limitations. No liquid products were detected for either CoPc/N-CNTs or CoPc/CNTs (Fig. 3a and Fig. S11), whereas CoPc/N-CNTs showed markedly superior CO_2-to-CO conversion performance. Below −0.78 V vs. RHE, CoPc/CNTs maintained an FEco comparable to that of CoPc/N-CNTs but with a significantly lower CO partial current density. At −1.18 V vs. RHE, CoPc/N-CNTs achieved a peak CO partial current density (j_{CO}) of −761 mA cm^{-2} with a 95.1% FE for CO, whereas CoPc/CNTs reached only −448 mA cm^{-2} with a 75.6% FE for CO (Fig. 3b). Concurrently, the hydrogen evolution reaction (HER) was suppressed on CoPc/N-CNTs, with FE_{H2} reduced to approximately 5%, whereas the FE_{CO} remained above 95% across all applied current densities. In situ differential electrochemical mass spectrometry (DEMS) revealed that CoPc/N-CNTs presented a lower onset potential for CO_2-to-CO conversion, approximately 50 mV lower than that of CoPc/CNTs (Fig. S12). We concluded that the axial coordination of nitrogen atoms to CoPc significantly improved the FE for CO_2-to-CO conversion at high current densities while concurrently lowering the overpotential. Furthermore, in situ X-ray absorption fine structure (XAFS) analysis confirmed that the Co sites in CoPc/N-CNTs and CoPc/CNTs remained monodispersed under the reaction conditions (Fig. 3c and Fig. S13).

The stability of CoPc/N-CNTs in the flow cell was also assessed. By applying a polytetrafluoroethylene (PTFE) emulsion for the hydrophobic treatment of the gas diffusion layer, as previously reported methodology [37], we mitigated electrowetting damage at the three-phase interface (Fig. S14), achieving stability exceeding 60 h at −100 mA cm^{-2} (Fig. 3d). This performance is notable among reported CoPc-based catalysts for CO_2-to-CO conversion (Fig. 3e and Table S2). The absence of detectable metal or oxide species in the XRD patterns and the unshifted peaks in the XPS spectra before and after the reaction of the CoPc/N-CNT catalyst indicated that the catalyst maintained structural stability during the CO_2RR process (Fig. S15).

2.3. Mechanism investigation

To determine how the axial coordination of nitrogen to Co alters the catalytic mechanism, we initiated kinetic analysis. First, we measured the hydrogen/deuterium kinetic isotopic effect (KIE). As shown in Fig. 4a, the KIE value for CoPc/CNTs is approximately 1.5, whereas for CoPc/N-CNTs, it remains close to 1 within the potential range of −0.36 to −0.46 V vs. RHE. This disparity suggests that the rate-determining step (RDS) for CoPc/N-CNTs is independent of proton involvement, in contrast to the proton-dependent RDS for CoPc/CNTs. Furthermore, we employed gas mixtures with different concentrations of CO_2 and Ar and analyzed the Tafel slope over a kinetic control range at different CO_2 partial pressures, recognizing that different CO_2 partial pressures can influence the Tafel slope when CO_2 is involved in the RDS [38]. We observed that the Tafel slope for CoPc/N-CNTs increased from 157 to 206 mV dec^{-1} as the CO_2 partial pressure decreased (Fig. 4b), indicating the participation of CO_2 in the RDS for CO_2-to-CO conversion. In contrast, the Tafel slope for CoPc/CNTs remained at approximately 159 mV dec^{-1} across various CO_2 partial pressures, suggesting that CO_2 does not participate in the RDS, which aligns with the KIE results. Overall, these findings indicate that the rate-determining step for CoPc/N-CNTs likely involves electron transfer to CO_2, forming $^*CO_2^-$, indicating an electron transfer (ET) step. In contrast, the CoPc/CNTs RDS involves the protonation of $^*CO_2^-$ (proton transfer, PT) rather than an ET step. The axial coordination of nitrogen alters the RDS of CoPc/N-CNT for CO_2 conversion to CO.

We further conducted in situ attenuated total reflection surface-enhanced infrared absorption spectroscopy (ATR-SEIRAS)

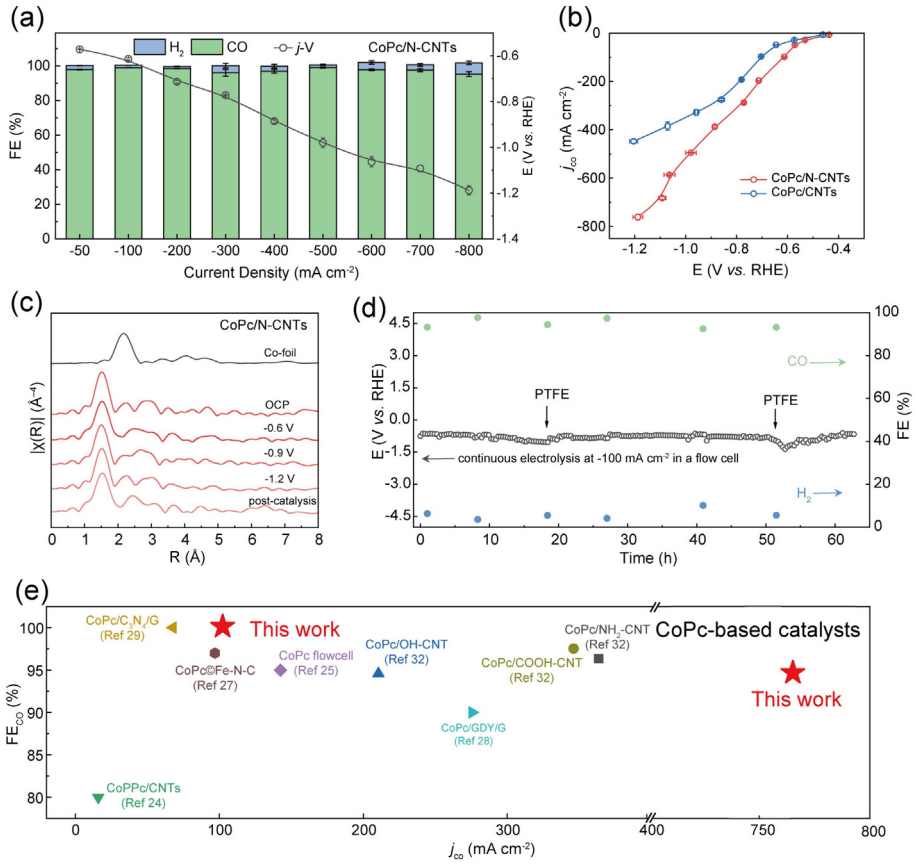

Fig. 3. (a) FEs of all CO_2RR products at different current densities and the corresponding *j-V* curves of CoPc/N-CNTs in a flow cell. (b) j_{CO} values of CoPc/N-CNTs and CoPc/CNTs. (c) In situ EXAFS spectra of CoPc/N-CNTs. (d) CO_2RR stability test of CoPc/N-CNTs at −100 mA cm^{-2}. Refresh the carbon paper with PTFE at the location indicated in the figure. (e) Performance metrics of different reported CoPc-based catalysts for CO_2-to-CO conversion.

to detect the adsorption behaviors of different species on the surface of the catalyst (Fig. 4c, d). The spectra revealed a broad peak between 1600–1700 cm^{-1}, corresponding to the O—H bending mode of water molecules. Notably, asymmetric peaks in the range of 1800–1900 cm^{-1} were observed, indicative of a linear Co—CO configuration [39]. Upon increasing the cathodic potential, a Stark effect-induced shift from 1838 to 1821 cm^{-1} was observed, reflecting a decrease in the resonant frequency due to the negative electric field [40]. The *CO peak was detected in both catalysts, and its peak area increased with increasing potential, indicating that it was deeply involved in the CO_2 electroreduction process. Furthermore, the *OH peak for CoPc/CNTs was larger than that for CoPc/N-CNTs, implying a lower water molecule coverage on the latter and thus a suppressed HER performance for CoPc/N-CNTs. Notably, the deviations in the *OH peak frequencies are attributed to the influence of surface coverage on vibrational band frequencies through dynamic dipole coupling [36].

To gain further insight into the mechanisms by which axial nitrogen coordination enhances CO_2RR activity on cobalt atoms, we conducted density functional theory (DFT) calculations. As illustrated in Fig. S16, models of two catalysts, CoPc/N-CNTs and CoPc/CNTs, were analyzed. The projected density of states (PDOS) results (Fig. S17) conclusively showed that the *d*-band center of Co atoms in CoPc/N-CNTs is positioned closer to the Fermi level than that in CoPc/CNTs is, directly indicating a stronger binding affinity for reactants on CoPc/N-CNTs. Moreover, charge density difference images (Fig. S18) for the active Co sites reveal significant changes, with blue regions indicating a decrease in charge density and yellow regions indicating an increase. Bader charge analysis further confirmed that Co atoms in CoPc/N-CNTs possess a lower charge density (+1.05 e versus +1.12 e in CoPc/CNTs), indicating an elevated electron density that strengthens bonding, in alignment with the PDOS findings. The reaction free energy diagrams (Fig. 4e, f) definitively illustrate that the energy barrier for CO_2 hydrogenation to *COOH is markedly reduced from 0.72 eV on CoPc/CNTs to 0.47 eV after axial N coordination, resulting in a significant increase in CO_2RR activity to CO on CoPc/N-CNTs. Although the merged ET and PT steps in the calculated *COOH hydrogenation process did not directly confirm a shift in the reaction's RDS, they demonstrated that axial N coordination significantly enhanced the CO yield on Co atoms in the CO_2RR.

In addition, analysis of the *CO reduction side reaction reveals that axial N coordination increases the energy required for *CO to *CHO (from −0.14 to −0.11 eV) and for *CHO to *CH_2O (from 0.51 to 0.55 eV), confirming that axial N coordination effectively hinders the side reaction. These results irrefutably demonstrate that axial N coordination to Co atoms not only improves the adsorption strength of reactants on Co atoms but also reduces the energy for *COOH formation to inhibit side reactions, thus significantly optimizing the CO_2-to-CO conversion process.

2.4. Membrane electrode assembly test

To advance practical applications, expanding the electrode area of CO_2 electroreduction is crucial for achieving higher CO yields. To this end, we employed a membrane electrode assembly (MEA) (Fig. S19). Initial evaluations using a 50 cm^2 MEA with a single piece of catalyst paper (Fig. 5a and Fig. S20) demonstrated the robust application potential of our catalyst. Remarkably, at a current density of −100 mA cm^{-2} and a total current of −5 A, the CO

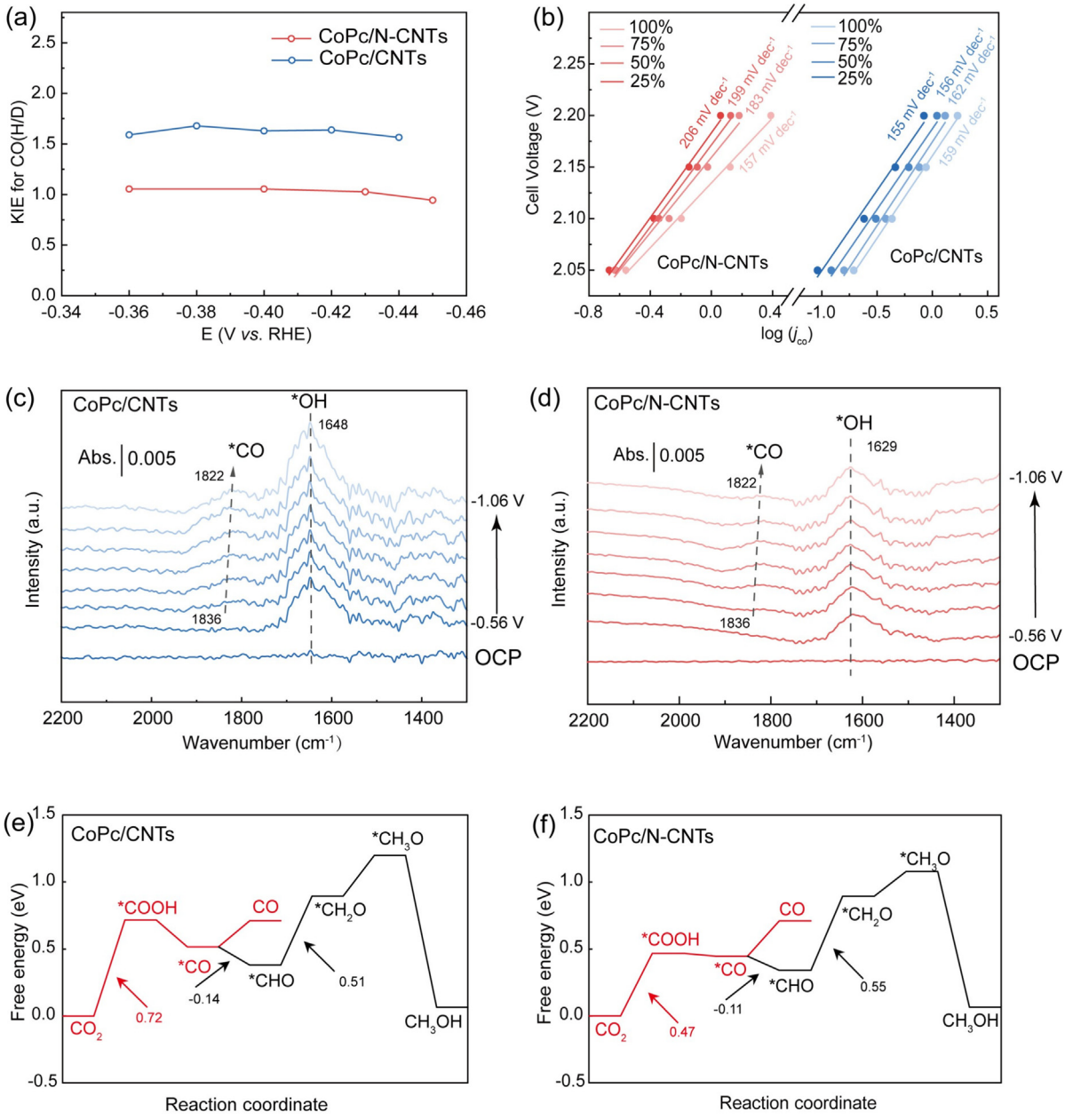

Fig. 4. (a) KIEs for CO over CoPc/N-CNTs and CoPc/CNTs. (b) Tafel slopes for CoPc/N-CNTs and CoPc/CNTs cathodes at different CO_2 partial pressures. (c, d) In situ ATR-SEIRAS spectra of CoPc/ CNTs and CoPc/N-CNTs. (e, f) Free energy of the CO_2RR for CoPc/CNTs and CoPc/N-CNTs.

FE remained constant at approximately 90% for over 20 h (Fig. 5b). To further increase the product yield, by alternating the cathode and anode, we configured a set of MEA units with four catalyst pieces, called tandem MEA (Fig. S21). Even at a higher current density of −300 mA cm^{-2} and a total current of −15 A, the catalyst sustained an impressive CO FE of 80% (Fig. S22). The cumulative CO partial current from the four electrodes reached −45.8 A (Fig. 5c), further underscoring the significant application potential of the CoPc/N-CNT catalyst. These results showed that CoPc/N-CNT catalysts exhibited outstanding performance in gas-phase electrochemical reactors, presenting a promising avenue for scaling up CO_2 reduction.

3. Conclusions

In summary, we have developed a Co–N_5 single-atom catalyst with axial nitrogen coordination that demonstrates exceptional activity and selectivity for the electrocatalytic reduction of CO_2 to CO. The obtained CoPc/N-CNT catalyst achieves outstanding performance, maintaining over 95% Faradaic efficiency at a CO partial current density of −761 mA cm^{-2}, significantly outperforming the CoPc/CNT catalyst. Mechanistic studies revealed that Co–N_5 active sites change the RDS, accelerating *COOH formation and increasing the free energy barrier for *CO reduction to CH_3OH, inhibiting further reduction. Additionally, the lower surface coverage of H_2O on CoPc/N-CNTs reduces the HER activity during the CO_2RR. Using an MEA reactor, CoPc/N-CNTs maintained 90% CO Faradaic efficiency for more than 20 h at −5 A. Scaling further achieved 80% CO efficiency at −15 A, highlighting its industrial potential. This work not only introduces a novel catalyst with exceptional CO_2-to-CO conversion efficiency but also integrates multiple advanced experimental techniques to elucidate the intrinsic mechanisms underlying its superior performance, paving the way for large-scale CO_2 electroreduction applications.

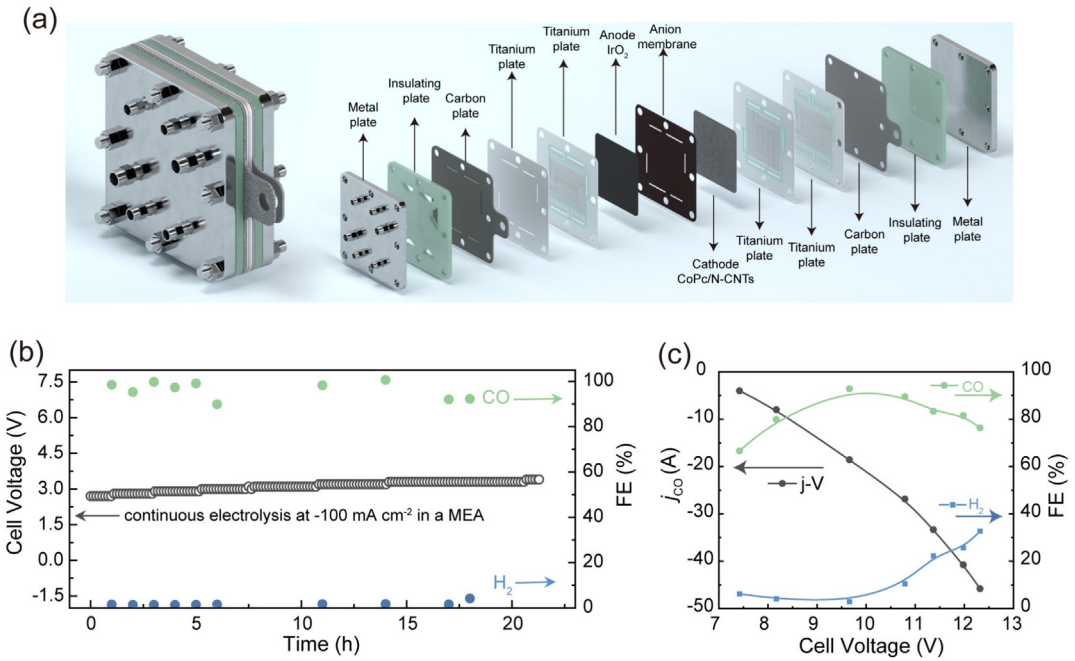

Fig. 5. (a) Photographs of the MEA device. (b) CO_2RR stability test of CoPc/N-CNTs at −100 mA cm^{-2} in MEA for a single piece of catalyst. (c) FEs of all CO_2RR products at different cell voltages and the corresponding *j-V* curves of CoPc/N-CNTs in a tandem MEA with 4 identical catalyst layers after integration.

Experimental section

Experimental details can be found in the Supporting Information.

CRediT authorship contribution statement

Yawei Hong: Writing – original draft, Investigation. **Chunxiao Liu:** Investigation. **Chengbo Li:** Investigation. **Haoyuan Wang:** Investigation. **Yuan Ji:** Investigation. **Xinyan Zhang:** Investigation. **Yujing Ren:** Investigation. **Zhaoyang Chen:** Investigation. **Qisheng Zeng:** Investigation. **Qiu Jiang:** Investigation. **Tingting Zheng:** Investigation. **Kun Jiang:** Investigation. **Xu Li:** Writing – review & editing, Project administration, Funding acquisition, Data curation. **Chuan Xia:** Writing – review & editing, Supervision, Funding acquisition, Conceptualization.

Data availability

All the data are available in the manuscript or the supplementary materials.

Declaration of competing interest

The authors declare the following financial interests/personal relationships which may be considered as potential competing interests: A China provisional patent application (2024115672503) based on the technology described in this work was filed in November 2024 by C. Xia, Y. Hong, T. Zheng and X. Li at the University of Electronic Science and Technology of China. The other authors declare no competing financial interests.

Acknowledgments

We acknowledge the National Key Research and Development Program of China (2022YFA1505700), the Fundamental Research Funds for the Central Universities (ZYGX2022J012), the NSFC (52171201, 22278067, 22322201, 22201272), the Central Government Funds of Guiding Local Scientific and Technological Development for Sichuan Province (2024ZYD0152), and the Natural Science Foundation of Sichuan Province (2025NSFJQ0017, 2024NSFSC1107, 2024NSFSC1104, 2023NSFSC0094). We appreciate the Analysis and Testing Center, University of Electronic Science and Technology of China, for their technical support. We thank beamline BL11B of the Shanghai Synchrotron Radiation Facility for providing the beamtime.

Appendix A. Supplementary material

Supplementary data to this article can be found online at https://doi.org/10.1016/j.jechem.2025.03.036.

References

[1] G.F. Manbeck, E. Fujita, J. Porphyr, Phthalocyanines 19 (2015) 45–64.
[2] B.A. Rosen, A. Salehi-Khojin, M.R. Thorson, W. Zhu, D.T. Whipple, P.J.A. Kenis, R. I. Masel, Science 334 (2011) 643–644.
[3] M. Liu, Y. Pang, B. Zhang, P. De Luna, O. Voznyy, J. Xu, X. Zheng, C.T. Dinh, F. Fan, C. Cao, F.P.G. De Arquer, T.S. Safaei, A. Mepham, A. Klinkova, E. Kumacheva, T. Filleter, D. Sinton, S.O. Kelley, E.H. Sargent, Nature 537 (2016) 382–386.
[4] J. Xue, X. Dong, C. Liu, J. Li, Y. Dai, W. Xue, L. Luo, Y. Ji, X. Zhang, X. Li, Q. Jiang, T. Zheng, J. Xiao, C. Xia, Nat. Commun. 15 (2024) 5998.
[5] M. Haake, D. Aldakov, J. Pérard, G. Veronesi, A.A. Tapia, B. Reuillard, V. Artero, J. Am. Chem. Soc. 146 (2024) 15345–15355.
[6] C. Kim, J.C. Bui, X. Luo, J.K. Cooper, A. Kusoglu, A.Z. Weber, A.T. Bell, Nat. Energy 6 (2021) 1026–1034.
[7] J.Y. 'Timothy' Kim, P. Zhu, F.-Y. Chen, Z.-Y. Wu, D.A. Cullen, H. Wang, Nat. Catal. 5 (2022) 288–299.
[8] J. Gu, S. Liu, W. Ni, W. Ren, S. Haussener, X. Hu, Nat. Catal. 5 (2022) 268–276.
[9] C. Xia, P. Zhu, Q. Jiang, Y. Pan, W. Liang, E. Stavitski, H.N. Alshareef, H. Wang, Nat. Energy 4 (2019) 776–785.
[10] L. Fan, C. Xia, P. Zhu, Y. Lu, H. Wang, Nat. Commun. 11 (2020) 3633.
[11] X. Kong, J. Zhao, Z. Xu, Z. Wang, Y. Wu, Y. Shi, H. Li, C. Ma, J. Zeng, Z. Geng, J. Am. Chem. Soc. 145 (2023) 14903–14911.
[12] S. Li, A.V. Nagarajan, X. Du, Y. Li, Z. Liu, D.R. Kauffman, G. Mpourmpakis, R. Jin, Angew. Chem. Int. Ed. 61 (2022) e202211771.
[13] Z.-H. Gao, K. Wei, T. Wu, J. Dong, D. Jiang, S. Sun, L.-S. Wang, J. Am. Chem. Soc. 144 (2022) 5258–5262.
[14] G. Deng, H. Yun, M.S. Bootharaju, F. Sun, K. Lee, X. Liu, S. Yoo, Q. Tang, Y.J. Hwang, T. Hyeon, J. Am. Chem. Soc. 145 (2023) 27407–27414.
[15] W. Deng, P. Zhang, B. Seger, J. Gong, Nat. Commun. 13 (2022) 803.

[16] S. Jin, Z. Hao, K. Zhang, Z. Yan, J. Chen, Angew. Chem. Int. Ed. 60 (2021) 20627–20648.
[17] Z. Chen, C. Wang, X. Zhong, H. Lei, J. Li, Y. Ji, C. Liu, M. Ding, Y. Dai, X. Li, T. Zheng, Q. Jiang, H.-J. Peng, C. Xia, Nano Lett. 23 (2023) 7046–7053.
[18] D. Zhao, Z. Zhuang, X. Cao, C. Zhang, Q. Peng, C. Chen, Y. Li, Chem. Soc. Rev. 49 (2020) 2215–2264.
[19] C. Chen, Y. Li, A. Huang, X. Liu, J. Li, Y. Zhang, Z. Chen, Z. Zhuang, Y. Wu, W.-C. Cheong, X. Tan, K. Sun, Z. Xu, D. Liu, Z. Wang, K. Zhou, C. Chen, J. Am. Chem. Soc. 145 (2023) 21273–21283.
[20] Y. Pan, R. Lin, Y. Chen, S. Liu, W. Zhu, X. Cao, W. Chen, K. Wu, W.-C. Cheong, Y. Wang, L. Zheng, J. Luo, Y. Lin, Y. Liu, C. Liu, J. Li, Q. Lu, X. Chen, D. Wang, Q. Peng, C. Chen, Y. Li, J. Am. Chem. Soc. 140 (2018) 4218–4221.
[21] W. Liu, Y. Liang, M. Huo, N. Ma, K. Qin, J. Chang, Z. Xing, Nano Res. 18 (2025) 94907195.
[22] Y. Bao, J. Xiao, Y. Huang, Y. Li, S. Yao, M. Qiu, X. Yang, L. Lei, Z. Li, Y. Hou, G. Wu, B. Yang, Angew. Chem. Int. Ed. (2024) e202406030.
[23] X. Zhang, Z. Wu, X. Zhang, L. Li, Y. Li, H. Xu, X. Li, X. Yu, Z. Zhang, Y. Liang, H. Wang, Nat. Commun. 8 (2017) 14675.
[24] N. Han, Y. Wang, L. Ma, J. Wen, J. Li, H. Zheng, K. Nie, X. Wang, F. Zhao, Y. Li, J. Fan, J. Zhong, T. Wu, D.J. Miller, J. Lu, S.-T. Lee, Y. Li, Chem 3 (2017) 652–664.
[25] S. Ren, D. Joulié, D. Salvatore, K. Torbensen, M. Wang, M. Robert, C.P. Berlinguette, Science 365 (2019) 367–369.
[26] Q. Feng, Y. Sun, X. Gu, Z. Dong, Electrocatalysis 13 (2022) 675–690.
[27] L. Lin, H. Li, C. Yan, H. Li, R. Si, M. Li, J. Xiao, G. Wang, X. Bao, Adv. Mater. 31 (2019) 1903470.
[28] H. Gu, L. Zhong, G. Shi, J. Li, K. Yu, J. Li, S. Zhang, C. Zhu, S. Chen, C. Yang, Y. Kong, C. Chen, S. Li, J. Zhang, L. Zhang, J. Am. Chem. Soc. 143 (2021) 8679–8688.
[29] Z. Wang, J. Yang, Z. Song, M. Lu, W. Wang, Z. Ren, Z. Chen, ACS Catal. (2024) 8138–8147.
[30] Y. Wu, Z. Jiang, X. Lu, Y. Liang, H. Wang, Nature 575 (2019) 639–642.
[31] X. Zhang, Y. Wang, M. Gu, M. Wang, Z. Zhang, W. Pan, Z. Jiang, H. Zheng, M. Lucero, H. Wang, G.E. Sterbinsky, Q. Ma, Y.-G. Wang, Z. Feng, J. Li, H. Dai, Y. Liang, Nat. Energy 5 (2020) 684–692.
[32] Q. Zhang, C.B. Musgrave, Y. Song, J. Su, L. Huang, L. Cheng, G. Li, Y. Liu, Y. Xin, Q. Hu, G. Ye, H. Shen, X. Wang, B.Z. Tang, W.A. Goddard, R. Ye, Nat. Synth. 3 (2024) 1231–1242.
[33] J. Su, C.B. Musgrave, Y. Song, L. Huang, Y. Liu, G. Li, Y. Xin, P. Xiong, M.-M.-J. Li, H. Wu, M. Zhu, H.M. Chen, J. Zhang, H. Shen, B.Z. Tang, M. Robert, W.A. Goddard, R. Ye, Nat. Catal. 6 (2023) 818–828.
[34] K. Xia, J.-H. Huang, L.-P. Ye, Water. Air. Soil Pollut. 233 (2022) 297.
[35] C.L. Rooney, M. Lyons, Y. Wu, G. Hu, M. Wang, C. Choi, Y. Gao, C. Chang, G.W. Brudvig, Z. Feng, H. Wang, Angew. Chem. Int. Ed. 63 (2024) e202310623.
[36] J. Li, H. Zeng, X. Dong, Y. Ding, S. Hu, R. Zhang, Y. Dai, P. Cui, Z. Xiao, D. Zhao, L. Zhou, T. Zheng, J. Xiao, J. Zeng, C. Xia, Nat. Commun. 14 (2023) 340.
[37] W. Fang, W. Guo, R. Lu, Y. Yan, X. Liu, D. Wu, F.M. Li, Y. Zhou, C. He, C. Xia, H. Niu, S. Wang, Y. Liu, Y. Mao, C. Zhang, B. You, Y. Pang, L. Duan, X. Yang, F. Song, T. Zhai, G. Wang, X. Guo, B. Tan, T. Yao, Z. Wang, B.Y. Xia, Nature 626 (2024) 86–91.
[38] Y. Wang, J. Kim, H.D. Jung, J. Liu, K. Ye, C. Xia, S. Back, K. Jiang, Nano Energy 127 (2024) 109728.
[39] X. Ren, J. Zhao, X. Li, J. Shao, B. Pan, A. Salamé, E. Boutin, T. Groizard, S. Wang, J. Ding, X. Zhang, W.-Y. Huang, W.-J. Zeng, C. Liu, Y. Li, S.-F. Hung, Y. Huang, M. Robert, B. Liu, Nat. Commun. 14 (2023) 3401.
[40] M. Moradzaman, G. Mul, ACS Catal. 10 (2020) 8049–8057.